

Unlocking cell chemistry evolution with operando fibre optic infrared spectroscopy in commercial Na(Li)-ion batteries

C. Gervillié-Mouravieff, C. Boussard-Plédel, Jiaqiang Huang, C. Leau, L. Albero Blanquer, M. Ben Yahia, M.-L. Doublet, S. Boles, X. Zhang, J. Adam, et al.

▶ **To cite this version:**

C. Gervillié-Mouravieff, C. Boussard-Plédel, Jiaqiang Huang, C. Leau, L. Albero Blanquer, et al.. Unlocking cell chemistry evolution with operando fibre optic infrared spectroscopy in commercial Na(Li)-ion batteries. Nature Energy, 2022, 7 (12), pp.1157-1169. 10.1038/s41560-022-01141-3 . hal-03850597

HAL Id: hal-03850597
https://hal.science/hal-03850597

Submitted on 14 Nov 2022

HAL is a multi-disciplinary open access archive for the deposit and dissemination of scientific research documents, whether they are published or not. The documents may come from teaching and research institutions in France or abroad, or from public or private research centers.

L'archive ouverte pluridisciplinaire **HAL**, est destinée au dépôt et à la diffusion de documents scientifiques de niveau recherche, publiés ou non, émanant des établissements d'enseignement et de recherche français ou étrangers, des laboratoires publics ou privés.



Distributed under a Creative Commons Attribution 4.0 International License

Unlocking cell chemistry evolution with in-operando fiber optic IR spectroscopy in commercial Na(Li)-ion batteries

C. Gervillié-Mouravieff[1,2], C. Boussard-Plédel[3], J. Huang[1,2,4], C. Leau[1,2], L. Albero Blanquer[1,2,5], M. Ben Yahia[6], M.-L. Doublet[6], S. T. Boles[7], X.H. Zhang[3], J.L. Adam[3] and J.-M. Tarascon[1,2,5,*]

[1] Collège de France, Chimie du Solide et de l'Energie—UMR 8260 CNRS, Paris, France.

[2] Réseau sur le Stockage Electrochimique de l'Energie (RS2E) - FR CNRS 3459, Amiens, France.

[3]Univ Rennes, CNRS, ISCR (Institut des Sciences Chimiques de Rennes) UMR 6226, F-35000, Rennes, France.

[4]The Hong Kong University of Science and Technology (Guangzhou), Sustainable Energy and Environment Thrust, Nansha, Guangzhou, Guangdong 511400, China.

[5]Sorbonne Université–UPMC Paris 06, Paris, France.

[6]ICGM, Univ Montpellier, CNRS, ENSCM, Montpellier, France

[7]Department of Energy and Process Engineering, Faculty of Engineering, Norwegian University of Science and Technology (NTNU), Trondheim, Norway.

* Corresponding author: J.-M. Tarascon: jean-marie.tarascon@college-de-france.fr

Abstract

Improvements to battery performance, reliability, and lifetime are essential to meet expansive demands for energy storage. As part of this, continuous monitoring of the dynamic chemistry inside cells offers an exciting path to minimizing parasitic reactions and maximizing sustainability. Building upon recent fiber optic-battery innovations, we report the use of operando infrared fiber evanescent wave spectroscopy to monitor electrolyte evolution in 18650 Na(Li)-ion cells under real working conditions. This approach enables identification of chemical species and reveals electrolyte and additive decomposition mechanisms during cycling, thereby providing important insights into the growth and nature of the solid-electrolyte interphase, the dynamics of solvation, and their complex interrelations. Moreover, by directly embedding fibers within the electrode material, we demonstrate simultaneous observations of both the material structural evolution and the Na(Li) inventory changes upon cycling. This illuminating sensing method has the power to reveal the otherwise opaque chemical phenomena occurring within each key battery component.

Introduction

Batteries play a central role in the ongoing transition from fossil fuels to renewable energy and are the versatile key enablers for the deployment of electric transportation, but their full acceptance is highly reliant on the ability of scientists to improve their autonomy, cost, lifetime, and safety[1]. Since chemical and electrochemical reactions are dynamical processes, these "living" devices suffer from multi-parameter degradation mechanisms leading, for instance, to the formation of the solid-electrolyte interphase (SEI) which often governs the life of the cell. Consequently, monitoring the intertwined electrolyte decomposition and SEI evolution is of paramount importance to understand and control the battery lifetime and safety. While operando techniques such as nuclear magnetic resonance (NMR), transmission electron microscopy (TEM), infrared (IR) or electron paramagnetic resonance (EPR) are powerful tools to access the microscopic scale[2–5], they are not readily translated out of laboratory test cells and into commercial-grade batteries. In this context, non-destructive diagnostic techniques, such as optical sensing, allow for real-time characterization with spatial resolution afforded by placing sensors directly inside cells [6,7]. Using optical fiber Bragg grating (FBG) sensors numerous parameters of interest can be measured, such as temperature (*T*), pressure (P) and strain (ε), with the feasibility of correlating these metrics to battery electrochemical behavior[8,9].

Moreover, using multiple sensors, we have even succeeded in tracking the heat associated with the formation of the SEI[10] and its dynamic evolution during cycling[11]. Although prolific, such approaches are ill-suited to capturing molecular insights occurring within each critical component of the battery, and the cascade of chemical reactions underlying the formation of the SEI. Aiming to close this gap, tilted fiber Bragg grating (TFBG) sensors offer a possibility for accessing additional observables (refractive index and turbidity) since by their nature, they allow for fiber guided light to interact with its local surroundings[12]. However, these sensors are still not capable of identifying individual molecular species.

Possible ways to overcome this limitation can be inspired by the field of spectroscopy and the use of UV-Vis, IR, and Raman activity ranges for chemical detection[13–15]. For instance, photonic crystal fibers (PCFs) are widely used in the development of biosensors for molecular recognition[16,17] and once paired with microfluidics, have recently been employed in the field of batteries to follow the evolution of electrolyte by Raman spectroscopy during cycling[18]. However, a weakness of the reported work is that it hinges on an external system (e.g. pumps and piping), preventing both continuous monitoring and the ability to track changes in the electrode materials themselves. Looking for other inspiration, we come across the use of fiber-based IR spectroscopy in the medical field[19–21]. Interestingly, even though this ex vivo approach can detect and follow severe liver disease via the detection of specific molecules, such an approach has never

been implemented with battery electrolytes or electrodes under real test conditions, where electrochemical potentials and reactive chemistries continually pose complex challenges.

Herein, we report in-operando IR fiber evanescent wave spectroscopy (FEWS) in commercial 18650 Na-ion cells and in Swagelok-type Li(Na)-ion cells. Since silica (SiO_2) optical fibers commonly employed in telecommunications are restricted to the 0.8 to 2 μm transmission region, we instead implement chalcogenide (sulfides, selenides, tellurides) glass fibers which have transmission windows ranging from 3 to 13 μm[22]. This opens a critical pathway to molecular identification and monitoring of the chemical dynamics occurring inside a cell during cycling. Hence, the method can provide evidence of the steps involved for SEI growth after cell manufacturing, as well as a means for tracking the Li(Na) inventory upon cycling (e.g., state od charge and state of health) and corresponding ion insertion kinetics. Such revelations highlight the emergence of a new era for rechargeable batteries, both in terms of chemical selection and cycling conditions.

Operando IR fiber evanescent wave spectroscopy

Fig. 1a shows the experimental setup for conducting fiber optic infrared detection via the use of $Te_2As_3Se_5$ (TAS) fiber. As depicted, absorption spectroscopy relies on the use of evanescent waves to probe molecular species at the fiber surface over a distance that depends upon the refractive index of the surrounding media (see calculation in Supplementary Fig. 1). Typical experiments are realized by passing the TAS fiber through a pre-drilled 18650 jelly-roll cell for the case of Na-ion (NVPF/HC) chemistry (Fig. 1a), or across a modified Swagelok cell (as described in Fig. 1b and c caption). The cells can then be connected to a Fourier transform infrared (FTIR) spectrometer equipped with a mercury-cadmium-tellurium (MCT) detector that collects IR-FEWS spectra while the cell is charged and discharged.

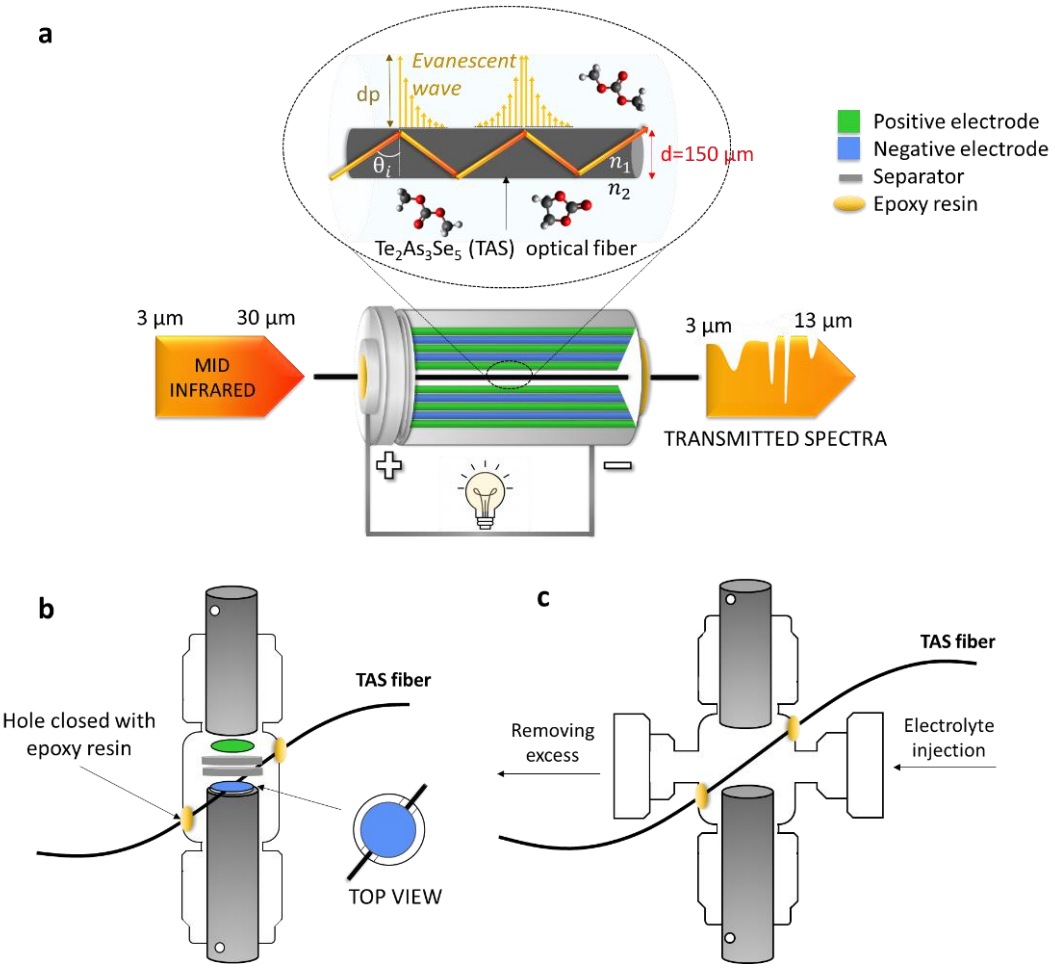


Fig. 1 | Integration of chalcogenide fiber into batteries. a, Schematic drawing of the mid-infrared light in the range from 830 to 5000 cm^{-1} propagating via internal reflections through the TAS fiber core (fiber diameter, d=150 µm). At the fiber surface, an evanescent wave is created, whose depth of penetration (dp, ~1 µm) is given by the relation[44,45]: $dp = \frac{\lambda}{2\pi\sqrt{n_1^2 \sin^2\theta_i - n_2^2}}$, where λ is the wavelength of the propagating light, θi the incident angle of the light, and (n1) and (n2), the refractive indexes of the fiber and of its surrounding medium, respectively. The TAS fiber is passing through the central void of a 18650 jelly-roll allowing IR-FEWS operando measurements of the electrolyte while cycling the battery. **b**, Two-electrode Swagelok cell modified for operando measurements. The body of the cell has been drilled with two hole so that the fiber can be embedded in the electrode material. **c,** Modified two-electrode Swagelok cell for acquisition of reference spectra. The Swagelok cell is drilled with two holes for the fiber to pass through, and two metal tubes terminated with rubber septa are welded to the cell body to inject solutions using syringes and evacuate the electrolyte while maintaining the inert atmosphere inside the cell core.

As a proof of concept, operando IR spectra recorded on a modified Swagelok cell (Fig. 1c) before and after adding the electrolyte are shown in Fig. 2a, and compared with reference spectra of the same solutions acquired with attenuated total reflectance spectroscopy (ATR) (Fig. 2b). As expected, no absorbance is observed in absence of electrolyte (considering the absorbance $A = \log\left(\frac{I_0}{I_s}\right)$ and $I_s = I_0$, with I_0 and I_s the transmitted intensity through the fiber with and without the sample, respectively). By contrast,

at each injection step, the IR bands characteristic of the added solutions appear concomitantly to their injection in the cell (Fig. 2a). This first result validates the use of TAS fibers to characterize electrolytes with a high molecular sensitivity (concentration less than 1%, see Supplementary Fig. 2) and fast response (4 seconds).

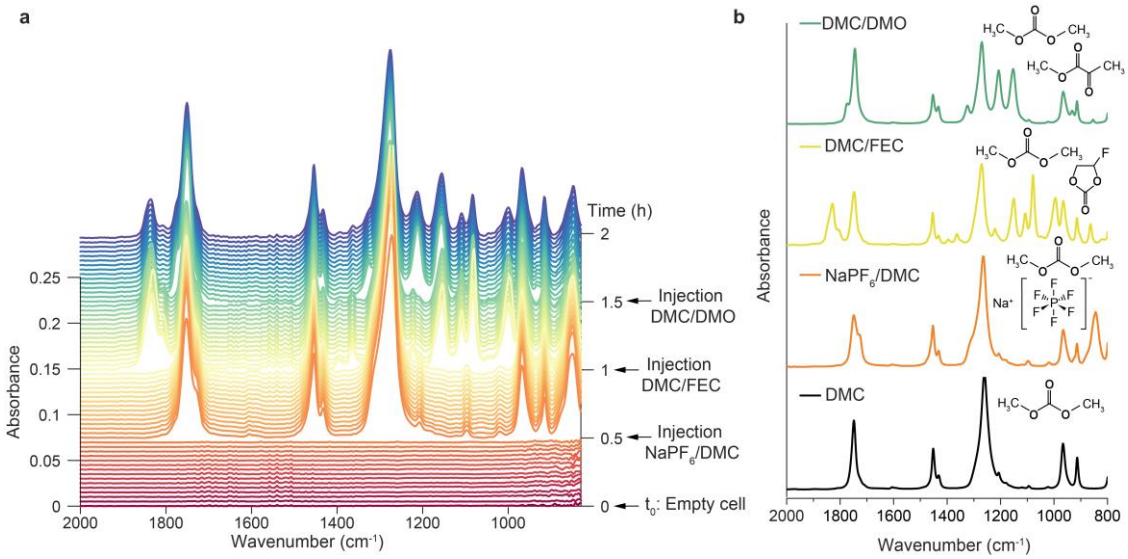


Fig. 2 | Online IR-FEWS measurement. a, Absorbance IR-FEWS spectra plot in function of time obtained via the use of a modified two-electrode Swagelok cell for hosting the TAS fiber. The IR-FEWS absorbance spectra were recorded every 120 s, with a resolution of 4 cm^{-1}, a number of scans of 16 and an acquisition time of 4 s. The acquisition starts at t=0 when the cell is empty, then every 30 minutes different solutions are added in the following order: 1 M $NaPF_6$ in dimethyl carbonate (DMC) ($NaPF_6$/DMC), DMC/FEC (1/1, v/v, DMC/FEC), and DMC saturated with DMO (DMC/DMO). **b**, Reference IR-ATR absorbance spectra of the different solutions injected during the experiment

Operando measurements of pure electrolyte mixture in 18650 cells

Before conducting operando measurements in 18650 cells, few considerations on the reliability of the measurement need to be addressed. Firstly, since the refractive index is function of temperature, this will also affect the penetration depth of the evanescent wave and hence the absorbance. Therefore it is essential to determine if temperature could affect our results, bearing in mind the range of temperature changes which can occur during battery cycling (see Supplementary Fig. 3 and 4). With temperature changes of 5°C, the measured changes in signal absorbance is 1% and the shifts in band positions are less than the spectrometer resolution, allowing us to safely neglect any temperature effect in exploiting future IR-FEWS data. Secondly, TAS fibers were installed into commercial NVPF/HC 18650 Na-ion cells and the inertness of the IR fiber was checked by monitoring the capacity retention of two cells with and without hosting fibers and by leaving the fibers in the electrolyte at 55 °C for one month (Supplementary

Figs. 5 and 6). Both cells show the same capacity retention at least up to 100 cycles, while SEM observations of the fiber stored in a harsh environment do not reveal any concerning visible change in fiber morphologies. Altogether, these results indicate that the nature of the fiber, together with the means of injecting it into the cell, have no discernable impact on the electrochemical process nor any interaction with the cell environment.

Having done these tests, we are ready to explore the potential of our optical IR-FEWS technique in a NVPF/HC 18650 cell with 1 M $NaPF_6$ in DMC ($NaPF_6$/DMC) electrolyte, which is known to be a mildly unstable system. In addition to the TAS fiber, a FBG sensor was incorporated in the cell to measure the internal temperature changes (ΔT) during cycling. Detailed working principle and calibration curves of the FBG are given in Supplementary Fig. 7).

The cycling data shown in Fig. 3a indicates an initial irreversibility as high as 80 mAh g_{NVPF}^{-1} between the first charge and discharge (≈160 mAh g_{NVPF}^{-1} and 80 mAh g_{NVPF}^{-1} capacities, respectively) indicative of copious electrolyte decomposition, in concert with a large temperature increase during the charge. To solely spot changes in the cell's evolving chemistry, the IR-FEWS absorbance spectra together with the relative evolution of absorbance $A(t)$-$A(t_0)$, after subtracting from the absorbance spectra $A(t)$ the reference absorbance at t=0 ($A(t_0)$) when the cell is first connected, were plotted in Fig. 3b,c and d.

During the first charge, a color change from green to dark blue is observed in Fig. 3b and is ascribed to the decrease of DMC absorption bands (see Supplementary Fig. 8 for DMC and $NaPF_6$ DMC reference spectra), while, at higher voltage, the change from green to yellow highlights the formation of products, confirming the expected decomposition of DMC. Turning to absorbance as a function of wavenumber (Fig. 3d), most of the bands corresponding to decomposition (negative band) and species formation (positive band), evolve during the first charge and can be attributed, according to the literature, to free and coordinated DMC, noted $DMC_{free.}$ and $DMC_{coor.}$, respectively (Fig.3c, d)[23]. Indeed, the solvation of Na^+ ions by the DMC molecules translates to a weakening of the C=O vibrational band of DMC resulting in a shift from 1753 cm^{-1} to 1732 cm^{-1} and in a strengthening of the O-C-O band associated with a shift from 1274 cm^{-1} to 1315 cm^{-1} (see Supplementary Fig. 8).

Interestingly, Fig. 3e highlights the asymmetric changes in the amplitude ratio of the free and solvated bands of DMC. This effect can be visualized within the νC=O absorption domain between 1700 cm^{-1} and 1800 cm^{-1} with the appearance of two peaks evolving in opposite directions: the positive shift, corresponding to the relative absorbance band of free DMC, has a smaller amplitude compared to the negative band shift corresponding to coordinated DMC. A similar effect is visible between 1150 cm^{-1} and 1400 cm^{-1} corresponding to the νOCO band of free and coordinated DMC. This indirectly indicates electrolyte dissolution involving both salt and solvent, which is confirmed by the decrease of the νPF band

at 850 cm^{-1} starting at the beginning of the charge and reaching a stable value before the end of charge (see Fig. 3e and ex-situ spectra in Supplementary Fig. 9). The νPF band no longer changes upon subsequent cycling or when the cell is left under open circuit voltage (see Supplementary Fig. 10) which indicates a partial, but irreversible, decomposition of $NaPF_6$ fully consistent with the presence of F^- based components (*e.g*, NaF) in the SEI, consistent with previously demonstrated XPS experiments on a similar NVPF/HC cell chemistry[24].

Besides these bands, we observe a broad band between 1600 cm^{-1} and 1700 cm^{-1} (indicated by a black dotted line in Fig. 3c,d) that grows upon charging and that could reasonably be assigned to the CO_2 asymmetric stretching mode of alkyl carbonate ($RCOO^-$). The large band width and low amplitude of the band being explained by the poor solubility alkyl carbonate in $NaPF_6$ DMC (see Supplementary Fig. 11). This confirms the well-known reacting pathway of electrochemical reduction of DMC[25,26] that can proceed via the cleaving of either the C-O or O-CH_3 bonds leading to alkyl carbonate and methoxy species, respectively. The absence for evidence of bands associated to Na-methoxy in our experiment may indicate that one bond cleavage is favored to the other under our experimental conditions.

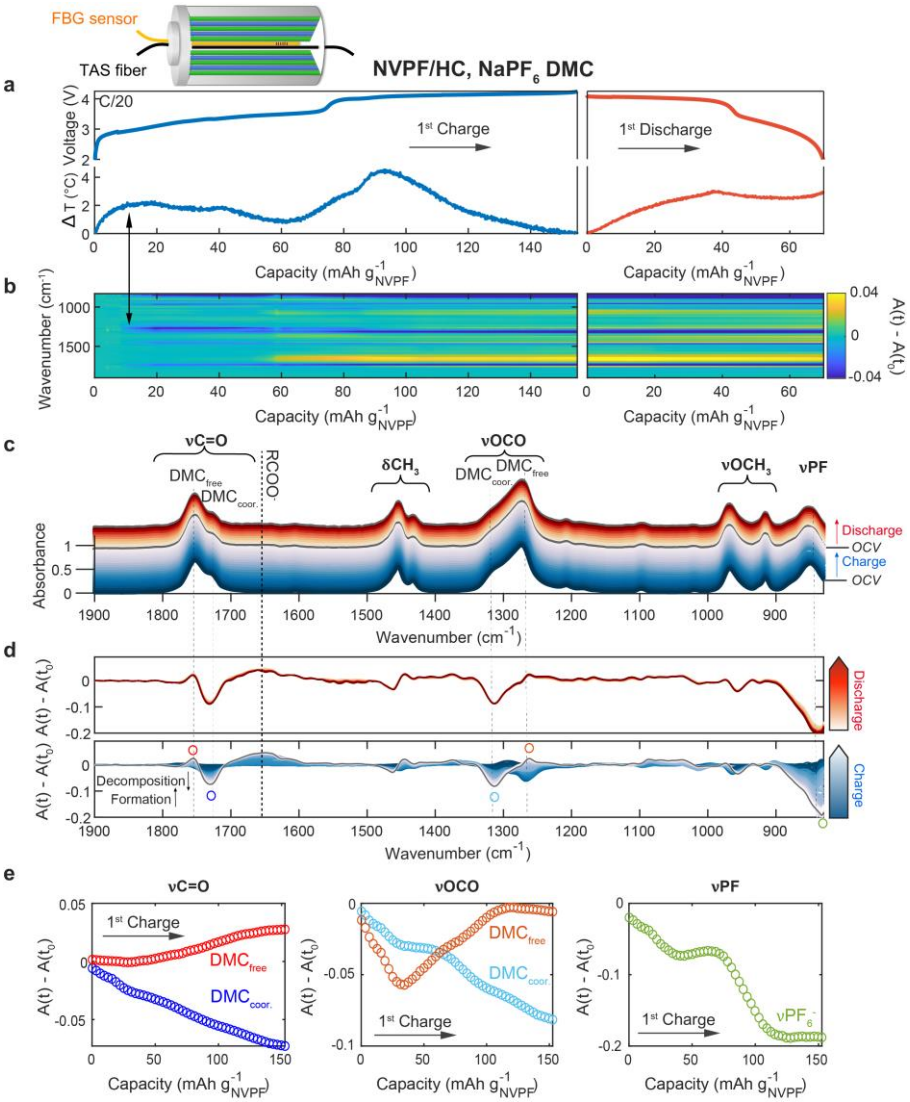


Fig. 3 | Operando IR-FEWS measurements of $NaPF_6$/DMC decomposition in 18650. **a**, Voltage (top) and temperature (bottom) change during the first charge (blue) and discharge (red) of NVPF/HC 18650 cell with $NaPF_6$/DMC electrolyte at C/20. **b**, Wavenumber versus capacity contour plot of the IR-FEWS operando absorbance spectra. The color change from green to yellow or blue implies a change in the relative evolution of absorbance $A(t) - A(t_0)$, as showed in the colorbar. **c**, Operando IR-FEWS spectra collected during the first charge with the colors of the spectra varying from blue in charge to red in discharge. Spectra collected during OCV are colored in gray. The notations $DMC_{coor.}$ and DMC_{free} refer to DMC molecules coordinated or uncoordinated to Na^+, respectively. **d**, $A(t) - A(t_0)$ relative absorbance evolution during charge (bottom, blue) and discharge (top, red). The formation of alkyl carbonate ($RCOO^-$) is highlighted by a black dotted line at 1650 cm^{-1}. The relative absorbance of the bands of interest at different wavenumbers during charge are indicated by a circle. Namely, νC=O of DMC_{free} (red), νC=O of $DMC_{coor.}$ (dark blue), νOCO of DMC_{free} (orange), νOCO of $DMC_{coor.}$ (light blue) and νPF of PF_6^- (green). **e**, $A(t) - A(t_0)$ relative absorbance evolution of the above-mentioned bands during the first charge. Note that prior to conducting operando IR measurements, the background was first collected (I_0) in atmosphere, with the fiber inserted into the cell before filling the electrolyte.

Binary electrolyte mixture

We now test the reliability of our technique by exploring a 18650 NVPF/C cell containing a binary electrolyte mixture (1 M $NaPF_6$ in ethylene carbonate-dimethyl carbonate (EC/DMC) (1/1, v/v)). Its capacity is shown in Fig. 4a together with the temperature evolution, revealing three peaks during the first charge and two peaks during the following discharge, in perfect agreement with our previous work[10] in which we correlated the larger temperature peak to electrolyte decomposition and SEI formation. The IR-FEWS absorbance spectra and relative absorbance $A(t) - A(t_0)$ plots are given in Fig.4b, c and d, with EC bands assigned according to reference spectra (Supplementary Fig. 8) and from previous studies[27]. Interestingly, the relative change in the IR contour plot (Fig. 4b) from blue to yellow confirms the formation of extra species with the appearance of several bands in the $A(t) - A(t_0)$ relative absorbance spectra (Fig. 4d).

The growth of these bands upon charge (indicated by purple stars) can be attributed to the dimethyl-2,5-dioxa-hexane carboxylate (DMDOHC) resulting from the well-known trans-esterification reaction between EC and DMC[25,28]. The DMDOHC bands absorption reach their maximum amplitude at the end of charge (and beginning of discharge; most likely due to incomplete reaction and delays in species diffusion) and then stabilize on the subsequent discharge (Fig. 4e), suggesting their participation in the formation of the SEI that is nearly completed at the first charge. In concert, the decrease of the νC=O band of EC at 1775 cm^{-1} (yellow circle) and the subsequent DMDOHC bands growth, confirm the EC involvement in the SEI formation (Fig. 4e).

Interestingly, the νC=O band of DMC is visible all along the charge process, although it may be partly hidden by the DMDOHC bands, proving the ability of EC to prevent DMC decomposition and is in line with the fact the solvent with the highest dielectric constant, EC, will decompose first.

As observed for the $NaPF_6$/DMC electrolyte, the νP-F band at 850 cm^{-1} decreases during the first charge and stabilizes during discharge (see Fig. 4f). In parallel, note the decrease and increase of the bonds corresponding to the νC-C vibration of the coordinated (1180 cm^{-1}) and uncoordinated (1164 cm^{-1}) EC ring, as expected due to the change in the salt concentration, associate to the degradation of $NaPF_6$ (Fig. 4f). Because of the fermi resonance of the EC molecule[29] this effect cannot be detected on the νC=O band stretching, but is confirmed by observing the solvation changes on the IR spectra of solutions at different concentrations of salt in EC/DMC, as shown in Supplementary Fig. 12. Finally, the broad band growth observed at 1675 cm^{-1} most probably pertains to a sodium alkyl carbonate and the one at 1033 cm^{-1} to sodium methoxide (indicated by black dotted line in Fig. 4c,d)[30]. However, the weak intensity of these bands together with their broadness do not allow a precise identification. This appearance of several new species in the electrolyte can be explained by the poor solubility of alkoxides and carbonates in DMC, as

opposed to EC/DMC, (see Supplementary Fig. 11), which is consistent with the greater dielectric constant of EC (ε = 89.7) compared to DMC (ε = 3.1).

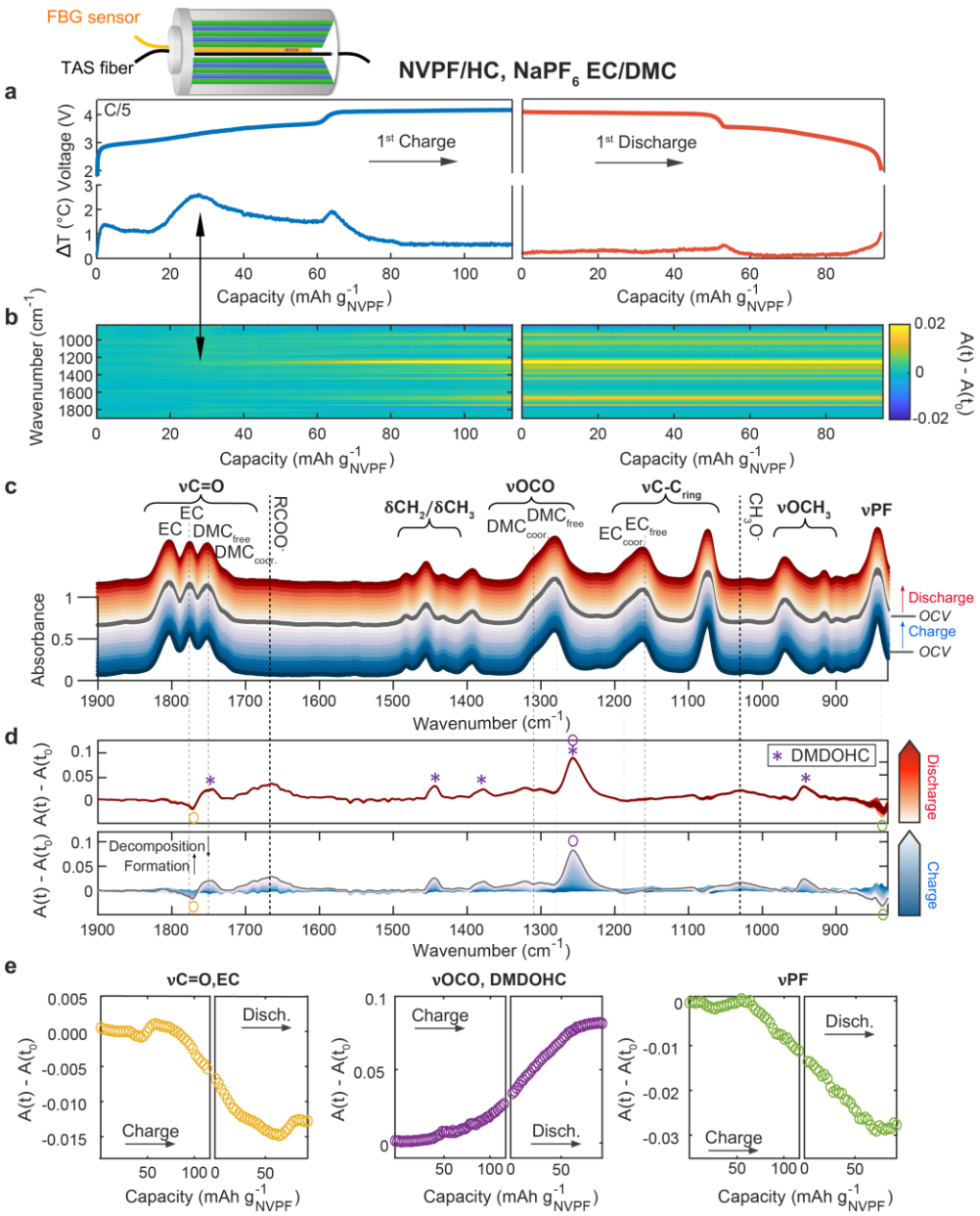


Fig. 4 | Operando IR-FEWS measurements of $NaPF_6$ EC/DMC decomposition in 18650. a, Voltage (top) and temperature (bottom) change during the first charge (blue) and discharge (red) of NVPF/HC 18650 cell with $NaPF_6$ EC/DMC electrolyte at C/5. **b,** Wavenumber versus capacity contour plot of $\Delta A(t\text{-}t_0)$ as a function of capacity. **c**, Absorbance spectra in function of charge (blue) and discharge (red). **d** $A(t) - A(t_0)$ relative absorbance spectra in function of charge (bottom, blue) and discharge (top, red). The formation of DMDHOHC, alkyl carbonate $RCOO^-$ and alkoxide CH_3O^- are highlighted by purple stars, black dotted line at 1675 cm^{-1} and black dotted line at 1033 cm^{-1}, respectively. The relative absorbance of the bands of interest at different wavenumbers are indicated by a circle. Namely, vC=O of EC (yellow), vOCO of DMDOHC (purple) and vPF of PF_6^- (green). **e**, evolution of the relative absorbance $A(t) - A(t_0)$ of the above mentioned bands during the first cycle.

Decomposition of vinylene carbonate additive

As a proof of concept, the decomposition of the vinylene carbonate (VC) additive was studied in NVPF/HC 18650 cells with 1 M $NaPF_6$ in EC/DMC (1/1, v/v) electrolyte with 3 wt% VC for two cycles at a C/5 rate (Fig. 5a). Reference spectra of VC and 1 M $NaPF_6$ in EC/DMC + 3 wt% VC are given in Supplementary Fig. 13 for comparison. The contour plot of the relative absorbance evolution, $A(t) - A(t_0)$ shown in Fig. 5b indicates that most of the chemical evolution occurs during the first charge and then stabilizes thereafter, in agreement with an important increase of the cell temperature, observed only during the first charge (see Fig. 5a).

The IR spectra and their relative evolution $A(t) - A(t_0)$ relative absorbance spectra are presented in Fig. 5b, c and d. The decomposition of VC is evidenced by the decrease in intensity of its band at 1834 cm^{-1} (Fig. 5e, bottom) corresponding to the νC=O stretching mode (black dotted line in Fig. 5c,d). Concomitantly, the derivative capacity dQ/dV shows the onset of a broad peak at 3.1 V during the first charge (Fig. 5e, top) that can be unambiguously ascribed to VC decomposition in light of previous studies on Na-ion NVPF/HC cells[24] and match perfectly with the largest peak in the thermal profile (Fig. 5e, middle). The νC=O band of VC decays during the charge, prior to reaching a plateau at the end of first charge (Fig. 5f). The absorbance of the νC=O band remains nearly constant upon the subsequent discharge and the following cycles, and the absence of any peak in the dQ/dV plot for the second charge confirms the general belief that VC contributes to the formation of a stable SEI during the first charge through the formation of an elastomer that prevents further electrolyte decomposition[31]. Interestingly, and in contrast to the previous case of binary mixtures, none of the characteristic bands of DMDOHC (1258 cm^{-1}) or sodium carbonate (1675 cm^{-1}) are detected, thus demonstrating the effectiveness of the additive[32].

In addition to the evolution of the VC bands upon charge, changes in the νC=O bands of free EC (1799 cm^{-1}) and free DMC (1749 cm^{-1}) are consistent with an overall decrease of PF_6^- in the electrolyte. As with the previous cases, the PF_6^- anion decomposes with a consequence on the solvent that is directly visible in the intensity decrease of the νOCO and νC-C modes corresponding to coordinated DMC and coordinated EC, and the concomitant increase of those corresponding to free molecules (Fig. 5f). Noteworthy here is the feasibility of observing a change in absorbance that matches the cycling behavior associated with a repeated change in the concentration of the coordinated cation complexes by switching from charge to discharge (see Fig. 5f). By changing the C-rate to 1C similar observations can be done, confirming the stability of the $NaPF_6$ EC/DMC + 3 wt% VC electrolyte (see Supplementary Fig. 14). In comparison, this situation was not spotted in presence of $NaPF_6$/DMC as the cell could not be cycled properly (see Supplementary Fig. 10).

These results demonstrate that operando IR-FEWS allows for longstanding open questions to finally be answered: What happens when a new additive is mixed with electrolyte? How do different molecules interact with each other in specific voltage ranges? Will a cell be sensitive to resting at a particular state of charge (SOC) after assembly? Nevertheless, at this stage, a further question arises regarding the applicability of this method to probing the electrode material itself, since the capability of these fibers may not be limited to liquids.

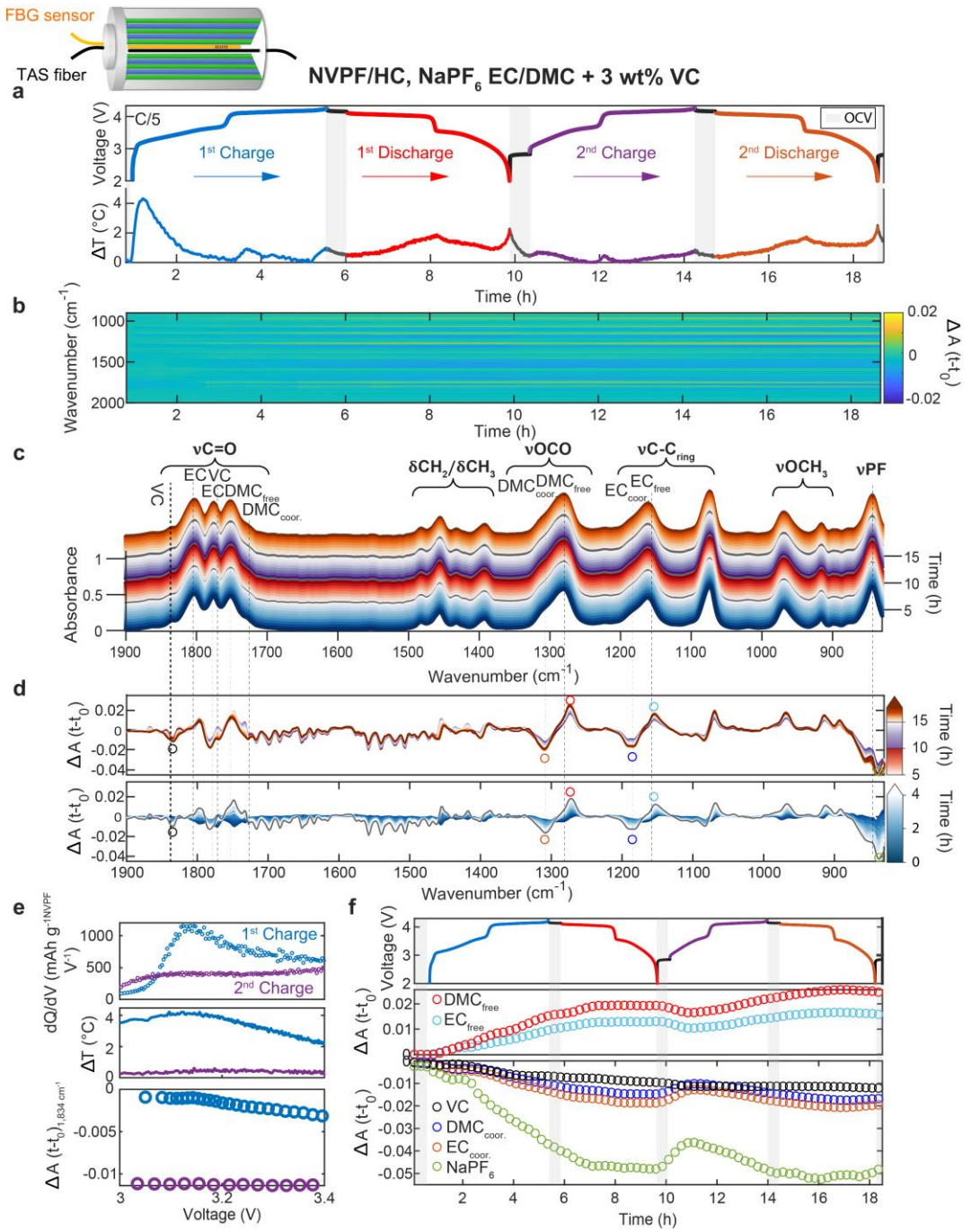


Fig. 5. | Operando IR-FEWS measurements of $NaPF_6$ EC/DMC + 3 wt% VC decomposition in 18650. **a**, Voltage (top) and temperature (bottom) change during the first charge (blue) and discharge (red) of NVPF/HC 18650 cell with $NaPF_6$ EC/DMC + 3 wt% VC electrolyte at C/5. **b**, Contour plot of the $\Delta A(t\text{-}t_0)$ spectra as a function of time. **c**, Absorbance spectra in function of the 1st charge (blue) 1st discharge (red), 2nd charge (purple) and 2nd discharge (orange). **d**, $A(t) - A(t_0)$ relative absorbance spectra in function of charge (bottom, blue) and discharge and the 2nd cycle (top, red, purple and orange). The bands of interest at different wavenumbers are indicated by a circle. Namely, vOCO of free DMC (red) and coordinated DMC (orange), vC-C_{ring} of free EC (light blue) and coordinate EC (dark blue), vPF of PF_6^- (green) and vC=O of VC (black). **e**, Differential capacity dQ/dV as a function of voltage between 3 and 3.5 V and intensity of the band at 1834 cm^{-1} (referenced by the black circle) versus voltage. **f**, $A(t) - A(t_0)$ relative absorbance evolution of the above-mentioned bands during the first two cycles plotted versus time.

Embedded and coated fiber

Among electrode materials, we chose to investigate $LiFePO_4$ (LFP) and $Na_3V_2(PO_4)_2F_3$ (NVPF) which are both IR active thanks to their PO_4 stretching modes located[33,34] between 900 cm^{-1} and 1200 cm^{-1}, and also commercially relevant today. The former is selected first, as it undergoes a single-step biphasic electrochemical process between two structurally well-defined end-members.

Prior to undertaking electrochemical testing, a TAS fiber was coated with LFP + carbon black (CB) + ethanol slurry, then dried prior to be immersed in a solution of I_2 in acetonitrile, which serves as a chemical oxidant (Fig. 6a). The IR spectra collected as a function of time spectacularly reflects the removal of Li according to the reaction $2LiFePO_4 + I_2 \rightarrow 2FePO_4 + 2LiI$ with the appearance of bands at 1237 cm^{-1}, 1095 cm^{-1} and 951 cm^{-1} upon delithiation (Fig. 6b,c) similar to those reported for $FePO_4$[35]. According to the simulated IR spectra, the lithiated and delithiated compounds have equivalent IR-active modes in the 900-1300 cm^{-1} region, therefore allowing a one-to-one correspondence of each mode, detailed in Supplementary Fig. 15. Thanks to this complete band assignment, the lithium extraction can be followed over time, providing new information on the reaction kinetics of LFP with I_2 (see Supplementary Fig. 16).

Next, a TAS fiber was embedded in the LFP+CB mixture and used as the positive electrode in a Li-half cell (Fig. 6d) using 1 M $LiPF_6$ in DMC as an electrolyte since its IR bands do not overlap with those of $LiFePO_4$. (see Supplementary Fig.17). Upon charge, the voltage profile yields a plateau at 3.6 V characteristic of the biphasic mechanism between $LiFePO_4$ and $FePO_4$ (Fig. 6e and Supplementary Fig.17a). As observed in Fig. 6f and g, the IR spectra recorded upon cycling exhibit progressive modification of the νPO_4 bands, similar to the change previously obtained with chemical oxidation (as well as *ex-situ* measurements provided in Supplementary Fig. 17c). Interestingly, the band evolution confirms the biphasic delithiation mechanism of LFP, with the intermediate spectra being a mixture of $LiFePO_4$ and $FePO_4$ spectra (an example for $Li_{0.5}FePO_4$ is given in Figure 6h). During discharge, the spectra reverse back to that of the pristine material (full cycle information is provided in Supplementary Fig.18), clearly evidencing the feasibility of tracking Li-intercalation and deintercalation processes in-operando and thereby enabling to track the Li-inventory during cycling and to access the cell's SOC (see Supplementary Fig.19). As a means of simplification, we demonstrate that similar results can be obtained using a fiber coated with LFP+CB and tested in the same electrochemical conditions (full cycle information is provided in Supplementary Fig. 20).

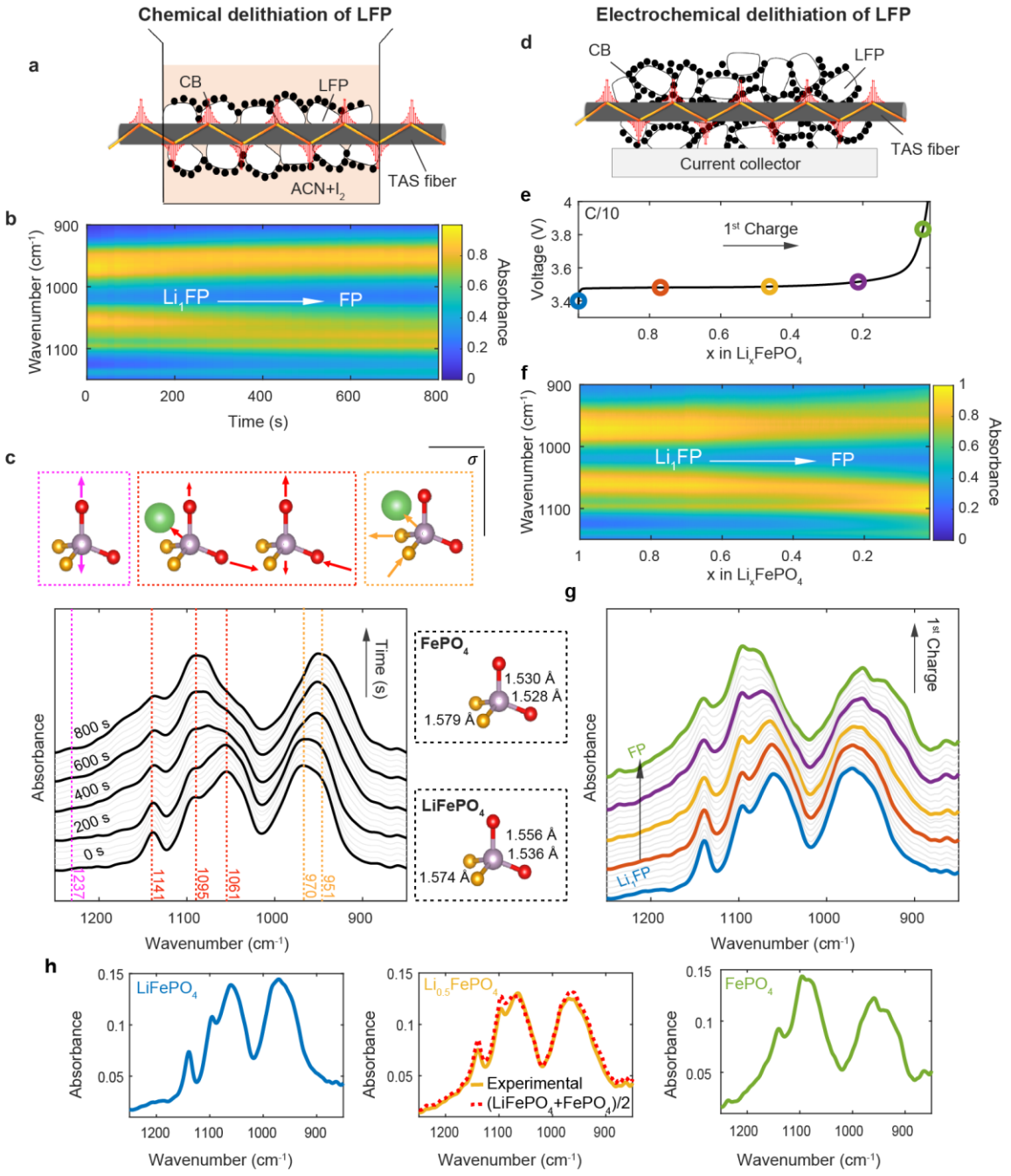


Fig. 6 | Operando IR-FEWS measurement of fiber coated and embedded in LFP. **a,** Schematic drawing of fiber coated with LFP + CB. The material is immersed at t = 0 s in a solution of acetonitrile (ACN) and iodine (I_2) in order to chemically delithiate the material. **b**, Contour plot of the absorbance spectra in the 800-1150 cm^{-1} region as a function of time. **c**, Stacked absorbance spectra of the coated fiber at 0 s, 200 s, 400 s, 600 s and 800 s. The PO_4 local structures of $LiFePO_4$ and $FePO_4$ are shown in the right blue and green panel respectively. For the olivine structure ($LiFePO_4$/$FePO_4$) two oxygen atoms (orange) share an edge with one FeO_6 octahedra and the two other ones (red) share a corner with two different FeO_6 octahedra. The vibration modes are indicated in top of the figure. **d**, Schematic drawing of the fiber embedded in an electrode of LFP + CB. **e**, First charge of LFP/Li cell with 1 M $LiPF_6$ in DMC as an electrolyte at C/10 up to 4 V. For an easy follow-up of the band evolution, circles have been added on the voltage profile and kept in the infrared spectra. **f**, Contour plot of the absorbance IR-FEWS spectra in the 800-1150 cm^{-1} region as a function of the lithium content x in Li_xFePO_4. **g,** Stacked absorbance IR-FEWS spectra at different value of the lithium content x. **h**, IR-FEWS absorbance spectra of $LiFePO_4$, $Li_{0.5}FePO_4$, $FePO_4$ obtained in operando by electrochemical delithiation, and calculated $Li_{0.5}FePO_4$ spectra using the average spectra of the two phases.

A TAS fiber embedded in a mixture of NVPF + CB was then used in order to track the Na uptake-removal in NVPF, which is known to undergo a multi-step electrochemical mechanism associated with phase transformations[36]. A Na/NVPF half-cell was assembled and cycled with 1 M $NaPF_6$ in DMC + 1 wt% of VC as an electrolyte and two plateaus at 3.7 V and 4.2 V corresponding to the extraction of two sodium ions, from Na_3VPF to Na_2VPF and from Na_2VPF to Na_1VPF, respectively (see Fig. 7a) become evident. The de-intercalation of sodium in Na_3VPF has been reported as a four-steps mechanism, including two different bi-phasic regions in the first plateau followed by one solid solution and one bi-phasic region in the second plateau [36]. The IR spectra corroborates this mechanism with the appearance of first a band at 937 cm^{-1}, followed by another one at 1084 cm^{-1} during the first Na removal. During the second Na removal, growing of broad bands at 998 and 937 cm^{-1} (see Fig. 7b,c) are observed, as well as shift of the band at 1084 cm^{-1}. The simulated IR-spectra shown in Supplementary Fig. 15 confirm the appearance of two new IR-active modes for the desodiated Na_1VPF in the 900-1000 cm^{-1} region which are assigned to the vibration of the Na-cages, and other PO_4 bands which are common to Na_3VPF and Na_1VPF. All these bands convert back to their initial position on the subsequent discharge, with the pre-charge spectrum being nearly identical to the post-discharge. Simultaneously, we spot only slight changes with the solvent absorption bands due to the dynamics of Na during intercalation and deintercalation, as well as the decomposition of the electrolyte (see Supplementary Fig. 21), further highlighting the sensitivity of the technique. Lastly, it worth mentioning that IR optical detection can also be used to track Li(Na) uptake-removal process in organic electrodes (see Supplementary Fig. 22).

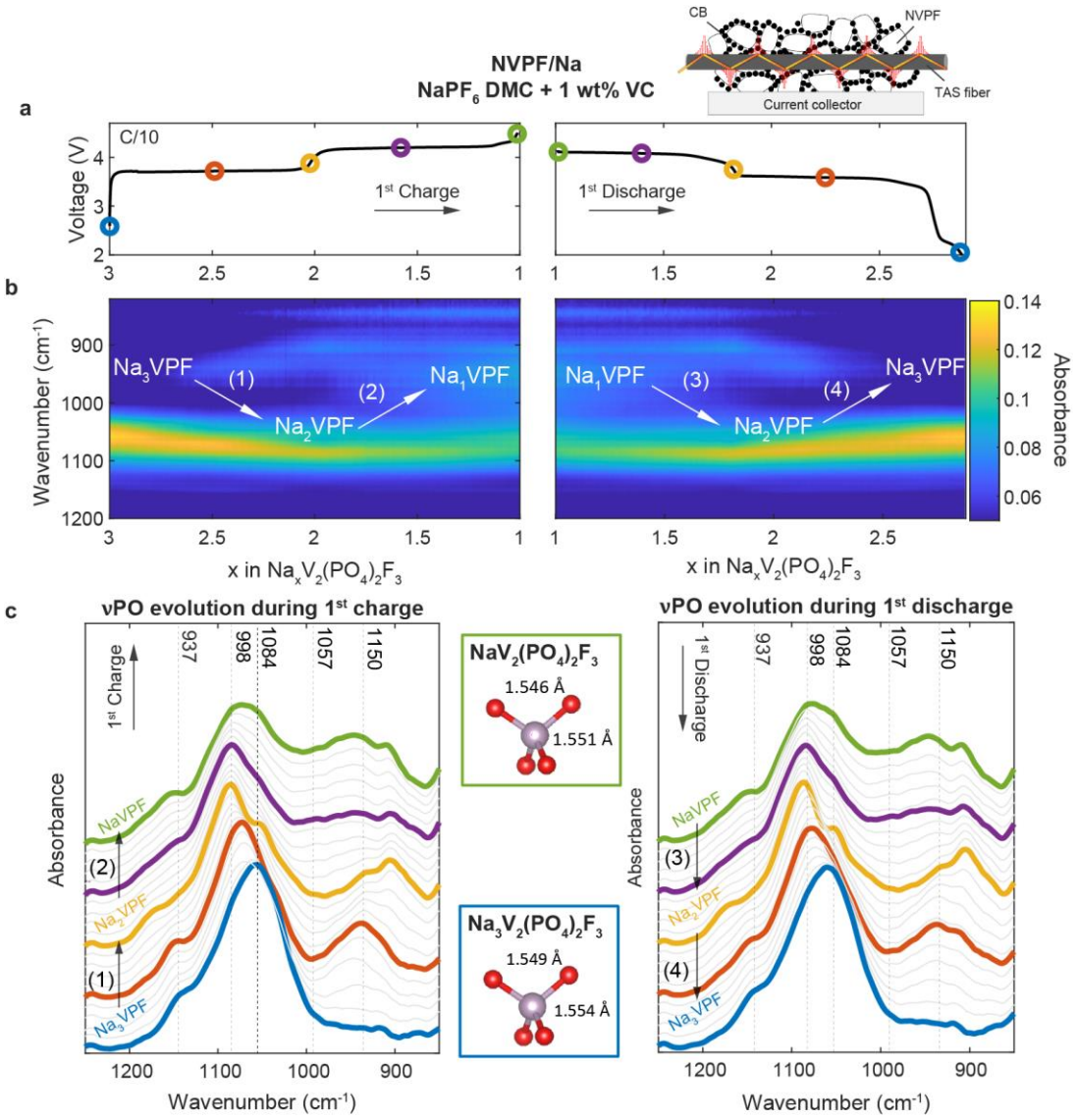


Fig. 7 | Operando IR-FEWS measurement of fiber embedded in NVPF. a, Schematic drawing of the experiment and voltage profile in function of the sodium content x in $Na_xV_2(PO_4)_2F_3$ during the first cycle of NVPF/Na cell with $NaPF_6$/DMC + 1 wt% VC as electrolyte at C/10 between 2 and 4.5 V. For an easy follow-up of the band evolution circles have been added on the voltage profile and kept in the infrared. **b**, Contour plot of the absorbance spectra in the 850-1200 cm^{-1} region as a function of the sodium content x during the first cycle. **c**, Stacked absorbance spectra in the 850-1200 cm^{-1} region at different value of the sodium content x following the color circle in the voltage curve, during the 1st charge (left) and the 1st discharge (right). Readers may note that the spectral changes observed around 850 cm^{-1} for the 1st cycle of NVPF with embedded fiber are incongruent with those observed previously and attributed to νPF. We humbly consider this to underscore the power of the IR-FEWS approach, as opposed to being an inconsistency. In each case, measurements are spatially localized to such an extent that the same spectral regions can be used to observe different physio-chemical phenomena, (*e.g.*, either in the electrolyte or in the electrode material) without need for complex decoupling approaches. The PO_4 local structures of Na_3VPF and Na_1VPF are shown in the blue and green panel respectively (see Supplementary Fig. 15 for calculated spectra and vibrations).

Altogether, such findings indicate that this approach is capable of following the intercalation and deintercalation processes of Li(Na) in battery materials and high carbon content composite electrodes, , thereby circumventing limitations of conventional ATR spectroscopy. Moreover, we were able to follow the decomposition of the electrolyte and the dynamics of the solvent within the same experiment, hence underscoring another advantage of operando IR-FEWS, since electrode and electrolyte interactions will always be interlinked and codependent on each other.

Conclusions

We have introduced an operando optical-fiber-based evanescent wave infrared spectroscopy relying on benign chalcogenide fibers for monitoring the evolving chemistry in commercial 18650 Na-ion batteries under operating real working conditions, which is a long-standing dream within the field of battery sensing. We demonstrate the validity of our technique by surveying the respective stability of electrolytes with various composition of solvents or additives. We successfully revealed changes in the dynamic of these solvents and additives without any latency, which enables us to identify the nature of the electrolyte decomposition species with excellent sensitivity as well as changes in the ion solvation dynamics as a function of the voltage and current. Through our study, we could verify the greatest instability of DMC versus EC-DMC or EC-DMC-VC based 1 M $NaPF_6$ electrolytes and similarly confirm the proposed decomposition mechanism that took years of conventional lab work to establish. Furthermore, we have shown the ability to track the potential at which a popular electrolyte additive, VC, is electrochemically reduced to stabilize the reduction of EC/DMC.

The in-depth assessment of this chemistry at the molecular level in the first formation cycle after cell manufacturing and onwards can be of great value to battery manufacturers, since this formation step is the “trade secret” for each company. The lack of any real-time diagnostic technique means that even in today’s best Li-ion cells, the routine for SEI formation is established by trial-and-error approaches. While any new information regarding the selection of cell currents and cell potentials during formation are helpful, unique identification of the molecular species participating in SEI nucleation and growth can translate into a new era for extending battery life.

In addition to the detection of the electrolyte, we proved the feasibility of following the Li uptake-removal process in carbon composite electrode materials by monitoring the IR-active modes of the P-O for LFP and NVPF, and C=O bond for the Li-terephthalate, bearing in mind that carbon is usually not a friendly element for IR spectroscopy. We can readily envision extending this study to other inorganic compounds like V_2O_5, $LiMnO_2$, and $LiCoO_2$ or to Li-rich transition metal oxides undergoing still unclear O-O bond reorganization upon cycling, provided that we slightly enlarge the transmittance window of the chalcogenide fiber. This calls for a deeper exploration of the chalcogenide glass design-space to enable

the probing of larger IR windows, in particular probing the M-O IR bands which are usually located around 16 µm.

Although we stress the added fundamental insights that IR-FEWS can offer to the battery community regarding the nature of the pertinent chemistries and molecular species, we are not yet offering a novel turnkey diagnostic technology. Nevertheless, immediate utilization from preliminary experimentation can be envisioned, either regarding formation cycle strategies or with guidance for handling and storage as a function of SOC and temperature. Turning to use in the field, although the fibers are insulating and chemically stable, there are several engineering limitations dealing with the brittleness of TAS fibers and the engineering of apertures in the cell. Such designs must avoid perturbing the venting valve and affirm airtightness, in the absence of any effect on long term performance (beyond the 100 cycles we have tried here). Additionally, different decomposition and formation reactions can induce counteractive effects on the infrared signal, hence making the deconvolution of the spectra complex without advanced data treatments. Methods based on machine learning could be one route to explore in order to quantify the different solvents during operando measurements[19–21]. Nevertheless, encouraging progress is already being made by the company DIAFIR that use fiber-based IR spectroscopy for medical diagnosis[19,20], and thus solutions for some complications might be found from synergistic efforts in other domains.

Lastly, we limited our concept demonstration to non-microstructured fibers, but we could envision that the same type of experiment with hollow core fibers could drastically increase the evanescent field penetration and enhance the sensitivity for IR detection. Noteworthy, compared to FBG sensing, one disadvantage of IR-FEWS is that we cannot host multiple distinct sensors in a single fiber segment, and we do not have multi-channel spectrometers, thus losing the multiplexing advantage. However, hope must prevail as ongoing studies are already utilizing the relatively quick spectrum acquisition time of IR-FEWS in combination with optical switches to enable a single IR channel to periodically monitor multiple fibers, hence enabling ageing studies and identification of ageing mechanisms. One envisioned scenario in the field would be to have a single battery module equipped with an IR-FEWS sensor, while the other modules in the pack could be considered as twins, and thus without the diagnostic hardware.

With the demonstration here of in-operando IR spectroscopy via optical TAS fibers, we see unprecedented opportunities for improved battery diagnostics under real working conditions. It is our hope that this technique opens what has long been considered a black box (chemistry-wise) to new insights that will rapidly enable the battery community to conquer challenges with formulating new electrolytes and optimizing battery formation protocols that govern battery lifetime and inevitably, its environmental impact.

Methods

Cells and electrode preparation. The 18650 NVPF/HC cells were provided dried and hermetically sealed without electrolyte by TIAMAT company. To test the inertness of the TAS fiber, cells with a single 0.8 mm hole was drilled in the center of the negative pole of the cell. The electrolyte is then injected in argon-filled glove box (<0.1 ppm H_2O and O_2) and the hole is closed with epoxy cured 12h. For the fiber embedded in the electrode, the active material powder $LiFePO_4$ (UMICORE) and $Na_3V_2(PO_4)_2F_3$ (made via a two-step ceramic process[37]) have been grounded around 10 minutes in a mortar with 10 wt% carbon black Super P (TIMCAL, Alfa Aesar) as a conductive agent. Next, a few droplets of ethanol were added to the powder and the slurry was placed on the fiber. For all the material the current collector was in stainless steel with a diameter of 19 mm. All electrodes were dried overnight in vacuum oven at 80 °C before transfer into the glove box.

Electrolyte preparation. In this work, the different sodium-based electrolytes used $NaPF_6$ (Stella Chemica) as the salt. The formulations were 1 M $NaPF_6$ in DMC (DMC, E-lyte, anhydrous, >99%), 1 M $NaPF_6$ in EC/DMC (EC, Mitsubishi Chemical) (1/1, v/v), and 1 M $NaPF_6$ in EC/DMC + 3 wt% VC (TINCI). For the lithium-ion cell, the electrolyte prepared is 1 M $LiPF_6$ (solvionic) in DMC + 1 wt% of VC (TINCI). The 1 M $LiPF_6$ in EC/DMC (LP30) have been provided by E-lyte.

Integration of fibers into the modified Swagelok for reference acquisition. The Swagelok cell (Ø 13 mm) was drilled with two holes of 0.45 mm for the fiber to pass through, and two metal tubes terminated with rubber septa were welded to the cell body to inject and evacuate the electrolyte while maintaining the inert atmosphere inside the cell core while adding and removing solutions. Then about 50 cm long TAS fiber was passed through the cell and attached on both external side with epoxy and cured for 12 h. The cell was closed in the glove box, taken out and attached to the spectrometer and detector, and the air-sensitive solutions were injected using syringes also prepared in the glove box.

Integration of fibers into the 18650. The 18650 cells were drilled with two holes of 0.8 mm on the center of the negative and positive sides of the cell to allow the fiber to pass through the central void of the jelly-roll. The drilled cell were dried under vacuum overnight at 80°C and introduced into the argon-filled glove box. Using a needle (Ø= 0.45 mm) as a guide, TAS fiber with a length of about 50 centimeters was passed through the cell. Once the fiber was placed with approximately the same length of fiber going out from each part of the cell, the hole on the positive electrode side was closed with epoxy and cured for 12h. Then, the fiber was connected to the spectrometer for background acquisition. Finally, in glovebox, about 5.3 ml of electrolyte was injected from the hole on the negative side and this hole was also sealed with epoxy and cured for 12 h. The cell was again connected to the spectrometer, to acquire the infrared spectra. In post-processing, the contribution of the epoxy to the infrared spectra was subtracted, allowing to have access only to the variations in the electrolyte.

Fiber embedded/coated into the electrode. The body of a Swagelok cell was drilled from side to side (Ø 19 mm) and a stainless steel current collector was used to apply the electrode slurry. The stainless steel plunger and current collector were aligned with the holes in the cell body so that the fiber would pass through the hole on top of the current collector. The fiber was fixed on both sides with cured epoxy for 12 hours and connected to the spectrometer once to acquire a background. Then, a droplet of the electrode formulation was deposited and spread on the surface of the fiber and the current collector. The entire assembly was finally dried overnight at 80°C in a vacuum oven.

In glovebox, the cell were assembled with two glass fiber separators (GF/D, Whatman) and a disk of lithium metal for LFP electrode and sodium metal for NVPF electrode.

For the coating, the fiber was first immersed for a few seconds in a slurry and air dried without contact on the previously immersed part. Then the fiber was passed through the cell and fixed with epoxy. The rest of the experiment proceeded as before.

IR-FEWS operando measurements. The operando measurements were realized with a Fourier transformed infrared spectrometer (T37 or Invenio S, Bruker) with an accessory connection system on the right side to focus the infrared beam on one entry extremity of the fiber. The MCT detector with a spectral range of 12000 - 600 cm^{-1} was used to record the optical signal at the output extremity of the fiber. During all the experiments, the MCT detector was cooled with liquid nitrogen. For all the experiments, the edges of the TAS fiber were cleaved manually. First, the fiber was marked perpendicular to the axis with a scalpel blade. Then, the fiber was pulled apart to produce a clean break. Finally, the edge was inspected with a fiber inspection scope (Thorlabs). The edge had to be flat, perpendicular and clean to have the beam going through the fiber with minimal loss. Then, using bare fiber terminator and multimode connectors the fibers were attached to the light source and the detector. The signal between the input and output of the fiber was controlled – amplitude around 10000 for 150 µm TAS fiber. The IR-FEWS spectra were acquired with 16 scans and a resolution of 4 cm^{-1} for a total acquisition time of 4 seconds. The spectra are recorded every 120 seconds during all the electrochemical tests. Note that the recording between the spectra was set at 120 seconds because it was not necessary to have more spectra at the C-rates used in this study. To minimize the atmospheric variations that directly affect part of the fiber outside the cell and the background, a tight Plexiglas box was used to protect all the setup. Thanks to this, a change in water absorbance of only 0.0004 was observed after 24 hours of measurements (see Supplementary Fig. 23).

Optical measurements with FBG. The FBGs used in the manuscript are provide by SAMYON Company and are 6 mm long, with a Bragg wavelength centered around 1,555 nm. The optical signals were acquired by FBGuard1550 (Safibra) interrogator, with a wavelength accuracy/resolution of 1 pm.

Calibration of FBG sensors. The temperature calibration of the FBG sensors was conducted in the temperature ovens (IPP55, Mermmet) from 35 to 15 °C in 5 °C increments and 4 h steps.

Electrochemical tests. Electrochemical properties were evaluated at room temperature by SP50 or MPG2 potentiostat (Biologic). The C-rate is calculated using the mass of active material of the positive electrode. The voltage window for NVPF/HC was 2.0 – 4.5 V, for NVPF/Na was 2.0 – 4.5 V, for LFP/Li was 3.0 – 4.0 V.

Chemical delithiation. The chemical delithiation was realized using a solution of iodine (99+%, Alfa Aesar) in acetonitrile (Sigma Aldrich). The amount of iodine was calculated to be in excess compared to $LiFePO_4$.

Computational details:

Calculations were performed using the CRYSTAL17 code [38–41] with all-electron atomic basis sets and the B3LYP functional for the exchange and correlation potential. Gaussian basis set of 6–11G, 86-411d41G, 85-21d1G, 8-511G, 86-411d4G, 8-411G, and 7-311 were employed to describe the Li, Fe, P, Na, V, O and F atoms. All atom coordinates and lattice parameters were fully relaxed using conjugate gradient energy minimization and the force tolerance for structural relaxation was set to 2.10–5 eV/Å. Vibrational frequencies were calculated within the harmonic approximation and the IR intensities were calculated using the CPKS method[42,43].

Data availability

The datasets generated during the current study are available in the article and its supplementary information. The data that support the plots within this paper are available from the corresponding authors upon reasonable request.

Acknowledgements

J.-M.T. acknowledges the International Balzan Prize Foundation and the LABEX STOREXII for funding. C.G. and J.-M.T. acknowledge Brurker for the instrumental setup. We thank TIAMAT for providing the NVPF/HC 18650 cells and R. Dugas for his assistance in the cell fabrication. We thank R. Chometon for the SEM images. MBY acknowledges the support of the French Agence Nationale de la Recherche (ANR) under reference ANR-17-CE05-10 (project VASELinA). STB acknowledges the support from the ENERSENSE research initiative (68024013) at the Norwegian University of Science and Technology (NTNU), Norway. Finally, we gladly thank S. Mariyappan, P. Desai and D. Larcher for valuable discussions and comments.

Author contributions

C.G. and J.-M.T. conceived the idea and designed the experiments with the help of C.B.P., J.-L.A., X.-H.Z. who provide the adequate fiber. C.G. performed the electrochemical, optical tests and the data analysis. MBY and M.-L.D conducted the theoretical analysis. C.B.P., J.H., L.A.B., S.T.B. C.L. X.-H.Z, J.-L.A. and J.-M.T. conjointly discussed the data and its meaning. Finally, C. G, M.-L.D. and J.-M.T., wrote the paper, with contributions from all authors.

Competing interests

A patent related to the work has been submitted (Application number: PCT/EP2022/071395) by the Centre National de la Rercherche Scientifique, Collège de France, Sorbonne Université, Université de Rennes 1, Ecole Nationale supérieure de Chimie de Rennes and Institut National des Sciences Appliquées de Rennes. The inventors are Jean-Marie TARASCON, Charlotte GERVILLIÉ-MOURAVIEFF, Catherine BOUSSARD, Xiang-Hua ZHANG and Jean-Luc ADAM. The patent cover a method for operando characterization of chemical species within a battery using infrared fiber evanescent wave spectroscopy.

Additional information

Correspondence and requests for materials should be addressed to Jean-Marie Tarascon.

Reference

1. Larcher, D. & Tarascon, J.-M. Towards greener and more sustainable batteries for electrical energy storage. *Nat. Chem.* **7,** 19–29 (2015).
2. Wang, F., Yu, H.-C., Chen, M.-H., Wu, L., Pereira, N., Thornton, K., Van der Ven, A., Zhu, Y., Amatucci, G. G. & Graetz, J. Tracking lithium transport and electrochemical reactions in nanoparticles. *Nat. Commun.* **3,** 1201 (2012).
3. Blanc, F., Leskes, M. & Grey, C. P. In Situ Solid-State NMR Spectroscopy of Electrochemical Cells: Batteries, Supercapacitors, and Fuel Cells. *Acc. Chem. Res.* **46,** 1952–1963 (2013).
4. Zhang, Y., Katayama, Y., Tatara, R., Giordano, L., Yu, Y., Fraggedakis, D., Sun, J. G., Maglia, F., Jung, R., Bazant, M. Z. & Shao-Horn, Y. Revealing electrolyte oxidation via carbonate dehydrogenation on Ni-based oxides in Li-ion batteries by in situ Fourier transform infrared spectroscopy. *Energy Environ. Sci.* **13,** 183–199 (2020).
5. Sathiya, M., Leriche, J.-B., Salager, E., Gourier, D., Tarascon, J.-M. & Vezin, H. Electron paramagnetic resonance imaging for real-time monitoring of Li-ion batteries. *Nat. Commun.* **6,** 6276 (2015).
6. Grey, C. P. & Tarascon, J. M. Sustainability and in situ monitoring in battery development. *Nat. Mater.* **16,** 45–56 (2016).
7. Huang, J., Boles, S. T. & Tarascon, J.-M. Sensing as the key to battery lifetime and sustainability. *Nat. Sustain.* **5,** 194–204 (2022).
8. Peng, J., Zhou, X., Jia, S., Jin, Y., Xu, S. & Chen, J. High precision strain monitoring for lithium ion batteries based on fiber Bragg grating sensors. *J. Power Sources* **433,** 226692 (2019).
9. Sommer, L. W., Raghavan, A., Kiesel, P., Saha, B., Staudt, T., Lochbaum, A., Ganguli, A., Bae, C.-J. & Alamgir, M. Embedded Fiber Optic Sensing for Accurate State Estimation in Advanced Battery Management Systems. *MRS Online Proc. Libr.* **1681,** 1–7 (2014).

10. Huang, J., Albero Blanquer, L., Bonefacino, J., Logan, E. R., Alves Dalla Corte, D., Delacourt, C., Gallant, B. M., Boles, S. T., Dahn, J. R., Tam, H.-Y. & Tarascon, J.-M. Operando decoding of chemical and thermal events in commercial Na(Li)-ion cells via optical sensors. *Nat. Energy* **5,** 674–683 (2020).
11. Desai, P., Huang, J., Hijazi, H., Zhang, L., Mariyappan, S. & Tarascon, J.-M. Deciphering Interfacial Reactions via Optical Sensing to Tune the Interphase Chemistry for Optimized Na-Ion Electrolyte Formulation. *Adv. Energy Mater.* **11,** 2101490 (2021).
12. Huang, J., Han, X., Liu, F., Gervillié, C., Blanquer, L. A., Guo, T. & Tarascon, J.-M. Monitoring battery electrolyte chemistry via in-operando tilted fiber Bragg grating sensors. *Energy Environ. Sci.* (2021). doi:10.1039/D1EE02186A
13. Manap, H., Dooly, G., O'Keeffe, S. & Lewis, E. Ammonia detection in the UV region using an optical fiber sensor. in *2009 IEEE Sens.* 140–145 (2009). doi:10.1109/ICSENS.2009.5398215
14. Michel, K., Bureau, B., Boussard-Plédel, C., Jouan, T., Adam, J. L., Staubmann, K. & Baumann, T. Monitoring of pollutant in waste water by infrared spectroscopy using chalcogenide glass optical fibers. *Sens. Actuators B Chem.* **101,** 252–259 (2004).
15. Yan, D., Popp, J., Pletz, M. W. & Frosch, T. Highly Sensitive Broadband Raman Sensing of Antibiotics in Step-Index Hollow-Core Photonic Crystal Fibers. *ACS Photonics* **4,** 138–145 (2017).
16. Cubillas, A. M., Unterkofler, S., Euser, T. G., Etzold, B. J. M., Jones, A. C., Sadler, P. J., Wasserscheid, P. & Russell, P. S. J. Photonic crystal fibres for chemical sensing and photochemistry. *Chem. Soc. Rev.* **42,** 8629–8648 (2013).
17. Bertucci, A., Manicardi, A., Candiani, A., Giannetti, S., Cucinotta, A., Spoto, G., Konstantaki, M., Pissadakis, S., Selleri, S. & Corradini, R. Detection of unamplified genomic DNA by a PNA-based microstructured optical fiber (MOF) Bragg-grating optofluidic system. *Biosens. Bioelectron.* **63,** 248–254 (2015).

18. Miele, E., Dose, W. M., Manyakin, I., Frosz, M. H., Ruff, Z., De Volder, M. F. L., Grey, C. P., Baumberg, J. J. & Euser, T. G. Hollow-core optical fibre sensors for operando Raman spectroscopy investigation of Li-ion battery liquid electrolytes. *Nat. Commun.* **13,** 1651 (2022).
19. Ellis, L. D., Buteau, S., Hames, S. G., Thompson, L. M., Hall, D. S. & Dahn, J. R. A New Method for Determining the Concentration of Electrolyte Components in Lithium-Ion Cells, Using Fourier Transform Infrared Spectroscopy and Machine Learning. *J. Electrochem. Soc.* **165,** A256 (2018).
20. Buteau, S. & Dahn, J. R. Analysis of Thousands of Electrochemical Impedance Spectra of Lithium-Ion Cells through a Machine Learning Inverse Model. *J. Electrochem. Soc.* **166,** A1611 (2019).
21. Corvec, M. L., Charpentier, F., Kachenoura, A., Bensaid, S., Henno, S., Bardou-Jacquet, E., Turlin, B., Monbet, V., Senhadji, L., Loréal, O., Sire, O., Betagne, J. F., Tariel, H. & Lainé, F. Fast and Non-Invasive Medical Diagnostic Using Mid Infrared Sensor: The AMNIFIR Project. *Innov. Res. Biomed. Eng.* **37,** 116 (2016).
22. Calvez, L. Chalcogenide glasses and glass-ceramics: Transparent materials in the infrared for dual applications. *Comptes Rendus Phys.* **18,** 314–322 (2017).
23. Cresce, A. V., Russell, S. M., Borodin, O., Allen, J. A., Schroeder, M. A., Dai, M., Peng, J., Gobet, M. P., Greenbaum, S. G., Rogers, R. E. & Xu, K. Solvation behavior of carbonate-based electrolytes in sodium ion batteries. *Phys. Chem. Chem. Phys.* **19,** 574–586 (2016).
24. Yan, G., Reeves, K., Foix, D., Li, Z., Cometto, C., Mariyappan, S., Salanne, M. & Tarascon, J.-M. A New Electrolyte Formulation for Securing High Temperature Cycling and Storage Performances of Na-Ion Batteries. *Adv. Energy Mater.* **9,** 1901431 (2019).
25. Eshetu, G. G., Grugeon, S., Kim, H., Jeong, S., Wu, L., Gachot, G., Laruelle, S., Armand, M. & Passerini, S. Comprehensive Insights into the Reactivity of Electrolytes Based on Sodium Ions. *ChemSusChem* **9,** 462–471 (2016).

26. Yan, G., Alves-Dalla-Corte, D., Yin, W., Madern, N., Gachot, G. & Tarascon, J.-M. Assessment of the Electrochemical Stability of Carbonate-Based Electrolytes in Na-Ion Batteries. *J. Electrochem. Soc.* **165,** A1222 (2018).
27. Angell, C. L. The infra-red spectra and structure of ethylene carbonate. *Trans. Faraday Soc.* **52,** 1178 (1956).
28. Yoshida, H., Fukunaga, T., Hazama, T., Terasaki, M., Mizutani, M. & Yamachi, M. Degradation mechanism of alkyl carbonate solvents used in lithium-ion cells during initial charging. *J. Power Sources* **68,** 311–315 (1997).
29. Nyquist, R. A. & Settineri, S. E. Infrared Study of Ethylene Carbonate in Various Solvents and Solvent Systems. *Appl. Spectrosc.* **45,** 1075–1084 (1991).
30. Pan, Y., Zhang, Y., Parimalam, B. S., Nguyen, C. C., Wang, G. & Lucht, B. L. Investigation of the solid electrolyte interphase on hard carbon electrode for sodium ion batteries. *J. Electroanal. Chem.* **799,** 181–186 (2017).
31. Aurbach, D., Gamolsky, K., Markovsky, B., Gofer, Y., Schmidt, M. & Heider, U. On the use of vinylene carbonate (VC) as an additive to electrolyte solutions for Li-ion batteries. *Electrochimica Acta* **47,** 1423–1439 (2002).
32. Sasaki, T., Abe, T., Iriyama, Y., Inaba, M. & Ogumi, Z. Suppression of an Alkyl Dicarbonate Formation in Li-Ion Cells. *J. Electrochem. Soc.* **152,** A2046 (2005).
33. Kosova, N. V. & Rezepova, D. O. Na1+yVPO4F1+y (0 ≤ y≤ 0.5) as Cathode Materials for Hybrid Na/Li Batteries. *Inorganics* **5,** 19 (2017).
34. Boivin, É. Crystal chemistry of vanadium phosphates as positive electrode materials for Li-ion and Na-ion batteries. (2017). at <https://tel.archives-ouvertes.fr/tel-03648931>
35. Ait Salah, A., Jozwiak, P., Zaghib, K., Garbarczyk, J., Gendron, F., Mauger, A. & Julien, C. M. FTIR features of lithium-iron phosphates as electrode materials for rechargeable lithium batteries. *Spectrochim. Acta. A. Mol. Biomol. Spectrosc.* **65,** 1007–1013 (2006).

36. Bianchini, M., Fauth, F., Brisset, N., Weill, F., Suard, E., Masquelier, C. & Croguennec, L. Comprehensive Investigation of the Na3V2(PO4)2F3–NaV2(PO4)2F3 System by Operando High Resolution Synchrotron X-ray Diffraction. *Chem. Mater.* **27,** 3009–3020 (2015).
37. Bianchini, M., Brisset, N., Fauth, F., Weill, F., Elkaim, E., Suard, E., Masquelier, C. & Croguennec, L. Na3V2(PO4)2F3 Revisited: A High-Resolution Diffraction Study. *Chem. Mater.* **26,** 4238–4247 (2014).
38. Becke, A. D. A new mixing of Hartree–Fock and local density-functional theories. *J. Chem. Phys.* **98,** 1372–1377 (1993).
39. Lee, C., Yang, W. & Parr, R. G. Development of the Colle-Salvetti correlation-energy formula into a functional of the electron density. *Phys. Rev. B* **37,** 785–789 (1988).
40. Erba, A., Baima, J., Bush, I., Orlando, R. & Dovesi, R. Large-Scale Condensed Matter DFT Simulations: Performance and Capabilities of the CRYSTAL Code. *J. Chem. Theory Comput.* **13,** 5019–5027 (2017).
41. Dovesi, R., Erba, A., Orlando, R., Zicovich-Wilson, C. M., Civalleri, B., Maschio, L., Rérat, M., Casassa, S., Baima, J., Salustro, S. & Kirtman, B. Quantum-mechanical condensed matter simulations with CRYSTAL. *WIREs Comput. Mol. Sci.* **8,** e1360 (2018).
42. Maschio, L., Kirtman, B., Rérat, M., Orlando, R. & Dovesi, R. Ab initio analytical Raman intensities for periodic systems through a coupled perturbed Hartree-Fock/Kohn-Sham method in an atomic orbital basis. I. Theory. *J. Chem. Phys.* **139,** 164101 (2013).
43. Maschio, L., Kirtman, B., Rérat, M., Orlando, R. & Dovesi, R. Ab initio analytical Raman intensities for periodic systems through a coupled perturbed Hartree-Fock/Kohn-Sham method in an atomic orbital basis. II. Validation and comparison with experiments. *J. Chem. Phys.* **139,** 164102 (2013).
44. Messica, A., Greenstein, A. & Katzir, A. Theory of fiber-optic, evanescent-wave spectroscopy and sensors. *Appl. Opt.* **35,** 2274–2284 (1996).
45. Lucas, J. Infrared glasses. *Curr. Opin. Solid State Mater. Sci.* **4,** 181–187 (1999).